Volume 14
Number 25
7 July 2023
Pages 6809–7088

Chemical Science

rsc.li/chemical-science

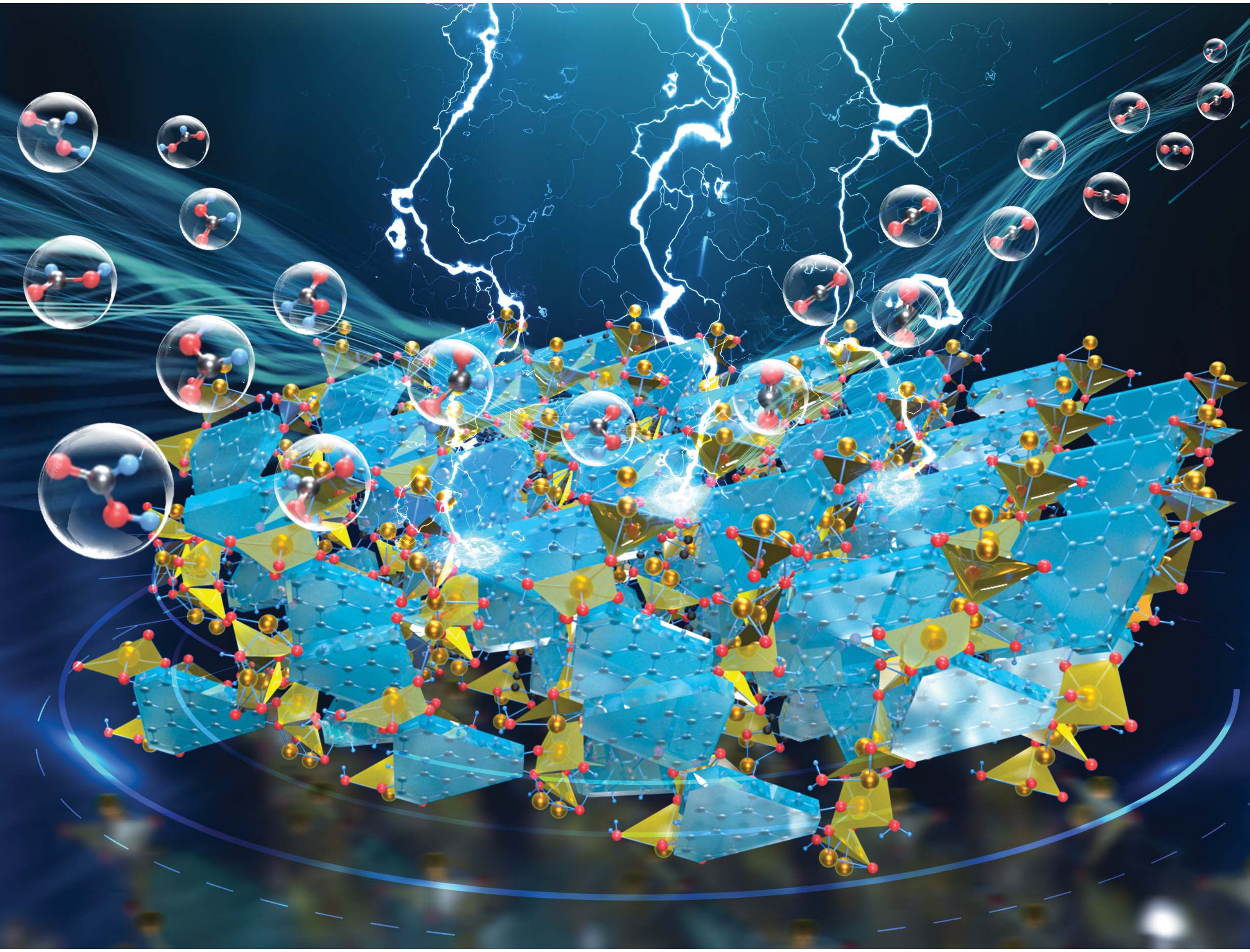

ISSN 2041-6539

EDGE ARTICLE
Wenjuan Yang, Zhicheng Zhang, Wenping Hu *et al.*
A conductive catecholate-based framework coordinated with unsaturated bismuth boosts CO_2 electroreduction to formate

Chemical Science

EDGE ARTICLE

View Article Online
View Journal | View Issue

Cite this: *Chem. Sci.*, 2023, **14**, 6860

Received 11th April 2023
Accepted 22nd May 2023

DOI: 10.1039/d3sc01876h

rsc.li/chemical-science

A conductive catecholate-based framework coordinated with unsaturated bismuth boosts CO_2 electroreduction to formate†

Zengqiang Gao,[a] Man Hou,[a] Yongxia Shi,[a] Li Li,[a] Qisheng Sun,[a] Shuyuan Yang,[a] Zhiqiang Jiang,[e] Wenjuan Yang,*[b] Zhicheng Zhang *[a] and Wenping Hu*[acd]

Bismuth-based metal–organic frameworks (Bi-MOFs) have received attention in electrochemical CO_2-to-formate conversion. However, the low conductivity and saturated coordination of Bi-MOFs usually lead to poor performance, which severely limits their widespread application. Herein, a conductive catecholate-based framework with Bi-enriched sites (HHTP, 2,3,6,7,10,11-hexahydroxytriphenylene) is constructed and the zigzagging corrugated topology of Bi–HHTP is first unraveled *via* single-crystal X-ray diffraction. Bi–HHTP possesses excellent electrical conductivity (1.65 S m^{-1}) and unsaturated coordination Bi sites are confirmed by electron paramagnetic resonance spectroscopy. Bi–HHTP exhibited an outstanding performance for selective formate production of 95% with a maximum turnover frequency of 576 h^{-1} in a flow cell, which surpassed most of the previously reported Bi-MOFs. Significantly, the structure of Bi–HHTP could be well maintained after catalysis. *In situ* attenuated total reflectance Fourier transform infrared spectroscopy (ATR-FTIR) confirms that the key intermediate is *COOH species. Density functional theory (DFT) calculations reveal that the rate-determining step is *COOH species generation, which is consistent with the *in situ* ATR-FTIR results. DFT calculations confirmed that the unsaturated coordination Bi sites acted as active sites for electrochemical CO_2-to-formate conversion. This work provides new insights into the rational design of conductive, stable, and active Bi-MOFs to improve their performance towards electrochemical CO_2 reduction.

Introduction

With ever-increasing global energy demand and the influence of climate change, the electrochemical CO_2 reduction reaction (CO_2RR) has attracted enormous attention for converting CO_2 into value-added fuels and feedstocks, which is not only a promising way to reduce the negative impact of climate change but also enriches energy supply and achieves net-zero CO_2 emission.[1,2] Formate, as one of the main CO_2RR products, has promising potential because of its compatibility with existing infrastructure and the promise for hydrogen storage and textile or leather production, proposing a carbon-neutral route to fuel generation.[3–6]

Electrocatalysts play a vital role in efficient CO_2-to-formate conversion.[4,7,8] Bismuth (Bi) with its low-cost and environment-friendly nature exhibits adequate adsorption intensity toward intermediate species for formate, attracting more and more attention.[9–11] Considering its low natural abundance and potential future large-scale applications, it is crucial to enhance the atomic utilization of Bi. Bi-based metal–organic frameworks (Bi-MOFs) with well-defined coordination and single-site dispersion are regarded as promising approaches to address this issue.[12,13] But their low electrical conductivity and saturated coordination mode remain significant obstacles to their performance and severely limit their broad application. Spectacularly, conductive MOFs (cMOFs) are deemed proactive materials for achieving excellent performance without the pyrolysis process owing to their distinctive electrical conductivity.[14–21] Despite the advances in the CO_2RR with cMOFs such as Cu-based cMOFs,[22–24] there is still a scarcity of literature on conductive Bi-MOFs for electrochemical CO_2-to-formate conversion with enhanced activity and satisfactory selectivity.

In this work, a three-dimensional (3D) Bi-based catecholate cMOF (Bi–HHTP) (HHTP, 2,3,6,7,10,11-hexahydroxytriphenylene)

[a]*Department of Chemistry, School of Science, Tianjin Key Laboratory of Molecular Optoelectronic Sciences, Tianjin University, Tianjin 300072, China. E-mail: zczhang19@tju.edu.cn; huwp@tju.edu.cn*

[b]*Julong College, Shenzhen Technology University, Shenzhen, 518118, China. E-mail: wj914315@163.com*

[c]*Haihe Laboratory of Sustainable Chemical Transformations, Tianjin 300192, China*

[d]*Joint School of National University of Singapore and Tianjin University, International Campus of Tianjin University, Binhai New City, Fuzhou 350207, China*

[e]*Vanadium and Titanium Resource Comprehensive Utilization Key Laboratory of Sichuan Province, Panzhihua University, Panzhihua, Sichuan 617000, P. R. China*

† Electronic supplementary information (ESI) available. CCDC 2242230. For ESI and crystallographic data in CIF or other electronic format see DOI: **https://doi.org/10.1039/d3sc01876h**

with enriched defects was fabricated for the CO_2RR and single-crystal X-ray diffraction verified its structure. Bi–HHTP with its robust nature could achieve optimal faradaic efficiency (FE) towards formate (95%) with a maximum turnover frequency (TOF) of $\sim$576 h^{-1}. *In situ* attenuated total reflectance Fourier transform infrared spectroscopy (ATR-FTIR) and density functional theory (DFT) calculations confirmed that the key intermediate is *COOH species. DFT calculations indicated that the unsaturated coordination Bi^{3+} sites could effectively facilitate the dissociation of *COOH to produce formate.

Results and discussion

Preparation and characterization

In this work, 3D Bi–HHTP was constructed *via* the solvothermal method (Fig. 1). Single-crystal X-ray diffraction (XRD) disclosed that Bi–HHTP exhibited a monoclinic type Bravais lattice ($\alpha, \gamma = 90°$ and $\beta = 143.57(2)°$) with space group $P2_1/n$. Intriguingly, the zigzagging corrugated chains of nonplanar ligands were coupled by the Bi–O bond (Fig. 1a–d), where each HHTP attached to seven Bi^{3+} ions at different angles (Fig. 1e) and the Bi^{3+} ion coordinated with the nonplanar catechol groups to form the unsaturated coordination mode (distorted tetragonal pyramid) (Fig. 1f). XRD patterns in Fig. 2a further confirmed the difference in Bi–HHTP, compared to traditional Ni–HHTP. No preferential orientation was found in Bi–HHTP. Thereafter, the conductivity of Bi–HHTP was measured by the two-contact probe technique. According to the current–voltage characteristic shown in Fig. 2b, Bi–HHTP exhibited an electrical conductivity of 1.65 S m^{-1}, which is higher than those of the reported MOFs as listed in Fig. 2c and Table S2.† Electron paramagnetic resonance spectroscopy (EPR) could effectively disclose the existence of unpaired electrons.[25] The EPR spectrum of Bi–HHTP (Fig. 2d) revealed a high-intensity peak at $g = 2.005$, verifying the presence of unpaired electrons located on defect sites. Transmission electron microscopy (TEM) and scanning electron microscopy (SEM) images showed that the morphology of Bi–HHTP was nanobelt-like (Fig. 2e, S1a and b†). The lattice fringes of Bi–HHTP in specific domains with lattice parameters of 0.18 nm matched well with [−4 −3 8] of Bi–HHTP (inset of Fig. 2e). The composition of Bi–HHTP was analyzed using the high-angle annular dark-field scanning transmission electron microscopy (HAADF-STEM) image and the corresponding energy-dispersive X-ray spectroscopy (EDS) elemental mappings (Fig. 2f), indicating the homogeneous distribution of Bi, C, and O elements.

Besides, UV-vis and FTIR were also employed to detect the feature of Bi–HHTP. The peaks of UV-vis spectra shown in Fig. 2g at $\sim$380 nm and $\sim$700 nm correspond to π–π^* and the ligand-to-metal charge transfer between the Bi^{3+} ion and HHTP.[26,27] Moreover, the peak at 685 cm^{-1} for FTIR shown in Fig. 2h was attributed to the vibration of the Bi–O entities, providing convincing evidence for forming Bi–HHTP.[16,28,29] Furthermore, we carried out *in situ* Raman tests to prove the robust stability of Bi–HHTP in 0.5 M $KHCO_3$ aqueous solution (Fig. 2i). The stretching mode of Bi–O entities was found at 313 cm^{-1}.[30] The peaks at around 1335 and 1582 cm^{-1} could be attributed to the characteristic defect (D) and graphitic (G) bands.[20,26,31] Remarkably, the unchanged Bi–O entities in $KHCO_3$ aqueous solution illustrated the robust structure of Bi–HHTP, compared to the reported Bi-based MOFs.[12,19]

Electrochemical performance

The CO_2RR performance was investigated in a flow cell (Fig. 3a) and the strong alkaline solution could enhance the conductivity of the electrolyte (0.194 S cm^{-1}, 1 M KOH) and lower the overpotential.[32,33] The liquid-phase products were detected by nuclear magnetic resonance (Fig. S4†). The polarization curves over Bi–HHTP in CO_2-purged cells shown in Fig. 3b illustrated a more positive onset potential and dramatically larger current densities than those in N_2-purged cells, signifying that Bi–HHTP could lower the reaction barriers for the CO_2RR. Inspiringly, the $FE_{formate}$ of Bi–HHTP shown in Fig. 3c could

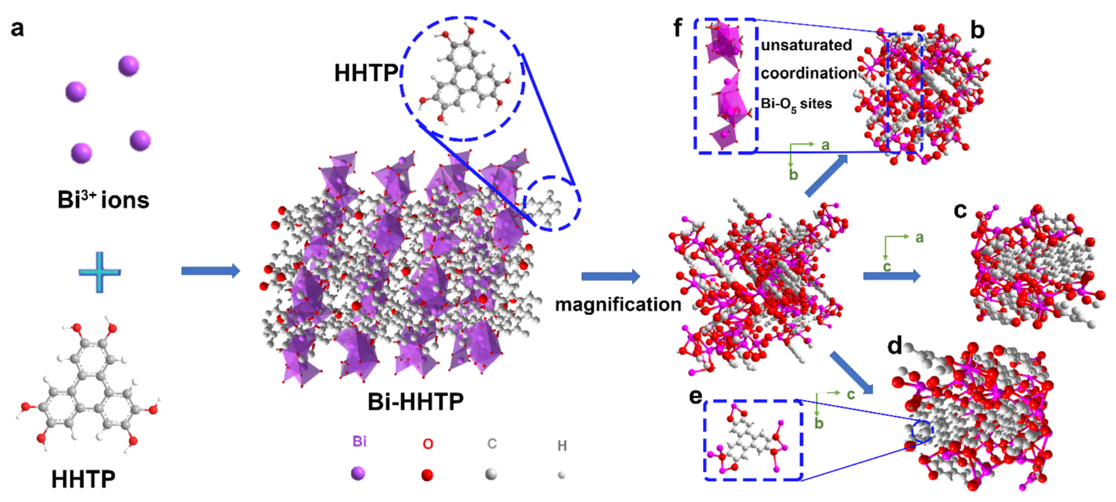

Fig. 1 (a) The general process for the synthesis of Bi–HHTP. (b–d) The views in a different dimension. (e) Chelation of HHTP toward Bi^{3+} ions. (f) The coordination environment of Bi^{3+} ions (distorted tetragonal pyramid).

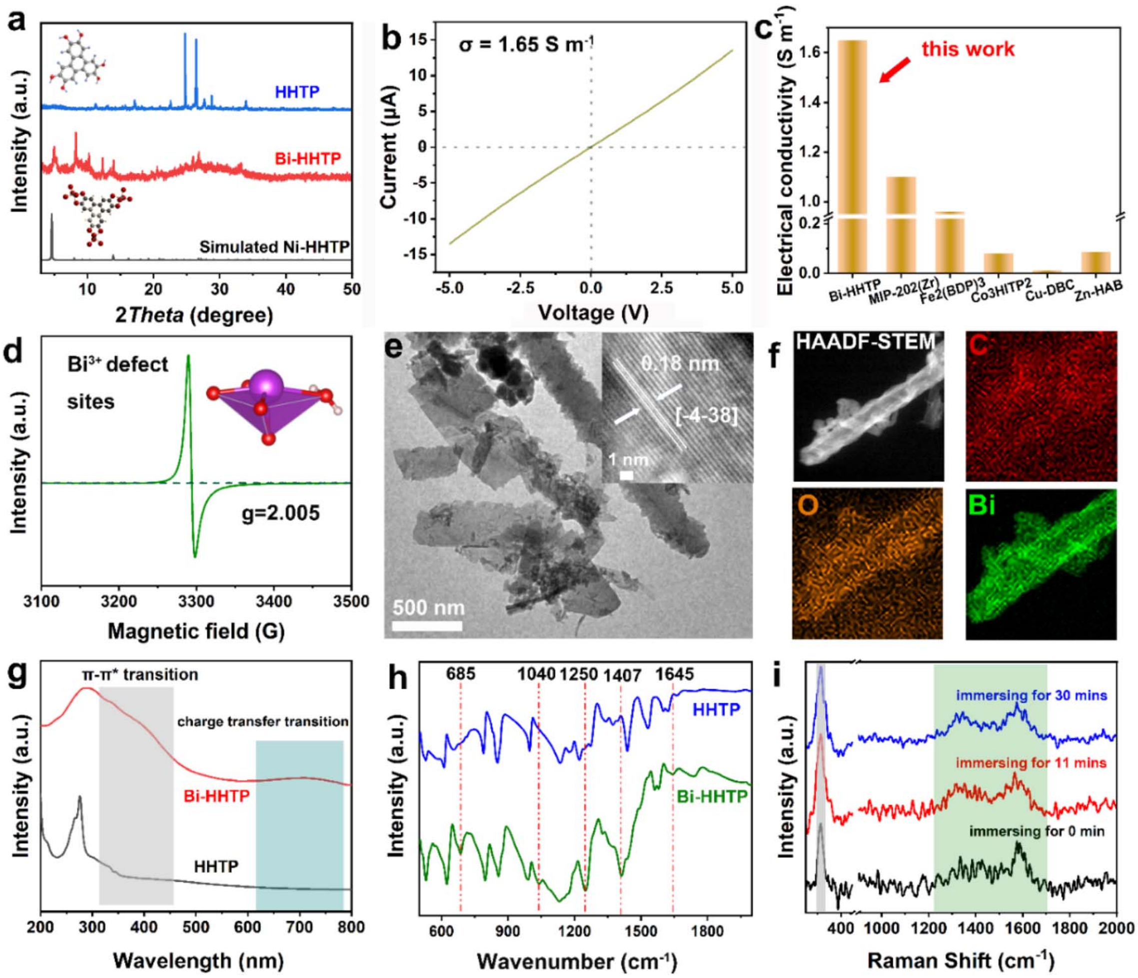

Fig. 2 (a) XRD patterns of Bi–HHTP and HHTP. (b) Current–voltage characteristic of Bi–HHTP using the two-contact probe method. (c) The compassion of conductivity of different MOFs. (d) EPR spectrum of Bi–HHTP. (e) TEM image, (f) HAADF-STEM image and the corresponding EDS elemental mappings of Bi–HHTP. (g) UV-vis spectra of Bi–HHTP and HHTP. (h) FTIR and (i) *in situ* Raman spectra of Bi–HHTP.

exceed 95% with a cathodic energy efficiency (CEE) of 68.8% at −0.7 V *vs.* RHE. The current density of Bi–HHTP was 93 mA cm^{-2} at −1.1 V *vs.* RHE.

Afterward, there was no discernible change in current density for over 30 h (Fig. 3d). The formate produced by Bi–HHTP at various potentials (Fig. 3e) illustrated that the generation rate could exceed 0.4 μmol s^{-1} and the TOF of Bi–HHTP could reach a maximum of 576 h^{-1}. Meanwhile, Bi–HHTP demonstrated a high FE of formate with a high current density, which outperforms most of the reported Bi-based or In-based materials (Fig. 3f and Table S3†). To boost the electrocatalytic activity of Bi–HHTP, this work also replaced the oxygen evolution reaction (OER) with the methanol oxidation reaction (MOR) (Fig. S9–S18†) to promote reaction kinetics. Inspiringly, the pair of CO_2RR//MOR systems only needed −1.9 V to achieve a current density of 10 mA cm^{-2}, much lower (about 400 mV) than that for the CO_2RR//OER (Fig. S19†). Moreover, the produced formate was quantitatively detected after electrolysis. Notably, the $FE_{formate}$ for the CO_2RR was over 90% from −2.1 to −2.5 V.

In situ ATR-FTIR spectroscopy and DFT calculations

To ascertain the intermediates and gain an understanding of the structure–performance relationship, *in situ* ATR-FTIR spectra were recorded and DFT calculations were applied. As shown in Fig. 4a, two FTIR signals at ∼1379 and 1410 cm^{-1} are assigned to the formation of *COOH species,[33] and the peak at 1643 cm^{-1} arises from the vibration frequency of the carboxylate ($^*CO_2^-$).[34–36]

The structural pattern of Bi–HHTP may be regarded as being composed of BiO_4–H_2O joined by organic linkers (HHTP). The Bi^{3+} ions have an unusual unsaturated coordination in their structure. As opposed to the saturated coordination of Bi^{3+} ions with six chemical bonds, the Bi site relates to four oxygen atoms and one water molecule (Fig. 4b). Fig. S20† illustrates the density of states of active Bi coordinative unsaturation. Four potential routes of unsaturated coordination Bi^{3+} sites for the CO_2RR are provided (paths 1–4 in Fig. 4c). Path 1 produces CO, paths 2 and 3 result in generating HCOOH, and path 4 is the hydrogen evolution reaction (HER) pathway. The active site is denoted

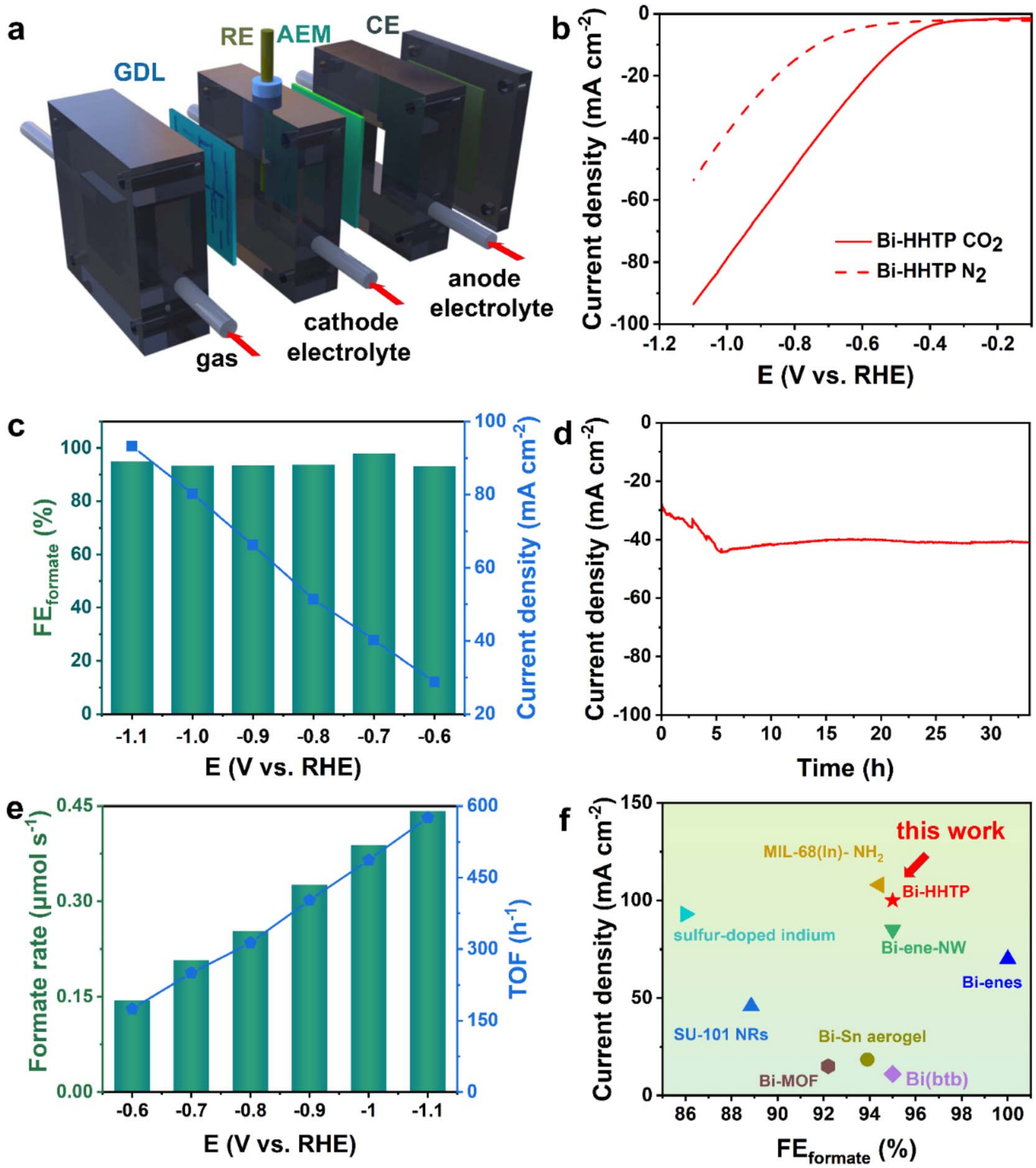

Fig. 3 (a) The illustration scheme of a liquid-phase flow cell device. (GDL, CE, RE, and AEM represent the working electrode, counter electrode, reference electrode, and anion exchange membrane, respectively) (b) LSV curves of Bi–HHTP in CO_2 and N_2 atmospheres without correction. (c) Potential-dependent formate FEs and current density of Bi–HHTP. (d) Stability test of Bi–HHTP at −0.7 V *vs.* RHE. (e) Formate rate and TOF of Bi–HHTP. (f) Comparison of our work with previously reported literature.

as H_2O* (* denotes the adsorption state) because the active Bi^{3+} sites were distorted tetragonal pyramids and one of the ligands is H_2O. In Fig. 4d, the energy profiles are displayed, showing that step II indicates the rate-determining step (RDS) and paths 1 and 2 are the best routes for producing HCOOH due to the lower RDS energy barrier (0.897 eV), compared to path 3 (1.15 eV) and path 4 (1.2 eV). Additionally, the blue value (path 1) is higher than the purple data (path 2). The HCOOH formation from step IV is preferable to CO generation, which is consistent with the *in situ* ATR-FTIR signals at ~1379 and 1410 cm^{-1}. The stronger selectivity for HCOOH shown between paths 1 and 2 is because *COOH on the Bi^{3+} site is strong enough to weaken the carbon–oxygen double bond. Path 4 for the HER has the highest energy barrier of 1.2 eV, which indicates that the generation of H_2 is unfavorable.[37] Therefore, the CO_2RR is preferable to the HER because CO_2 is easier to adsorb than H. The charge difference of every active species (*COO, *COOH, CO + H_2O, HCOOH, *OCO, *OCHO, *HCOOH, and *H) on the catalyst surface is displayed in Fig. 4e. The yellow part indicates the charge accumulation and cyan part illustrates the charge depletion. Much charge transfer could be found between the unsaturated coordination Bi^{3+} sites and active species. The experimental *in situ* ATR-FTIR results and the DFT data both show that Bi–HHTP exhibits a strong selectivity for HCOOH production.

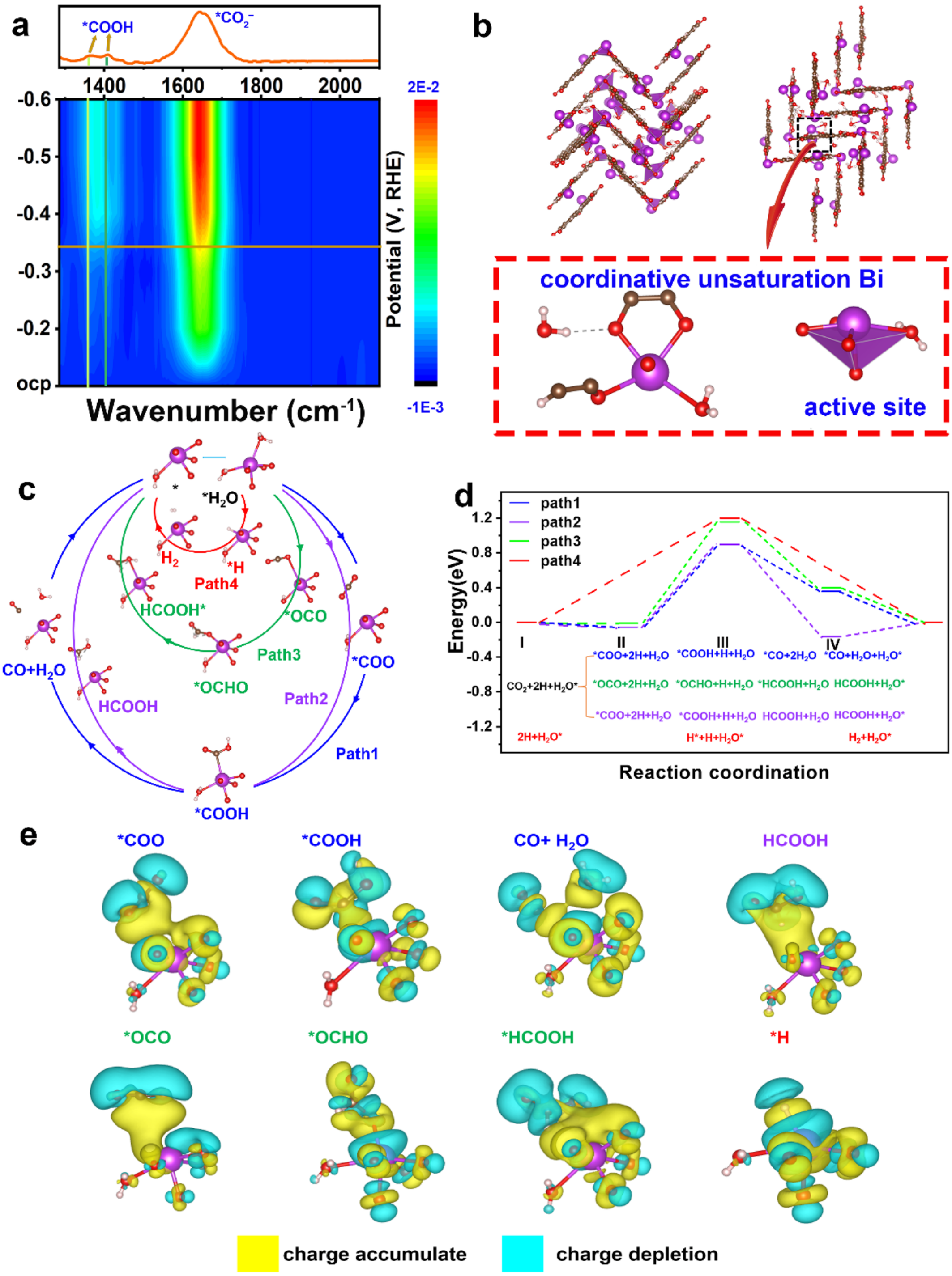

Fig. 4 (a) *In situ* ATR-FTIR spectra in CO_2-saturated 0.5 M $KHCO_3$ at applied potentials. (b) The active site Bi coordinative unsaturation with 4 oxygen atoms and one H_2O molecule bonded. (c) Four proposed reaction pathways on the active site to different products corresponding to the CO_2RR and HER. (d) The energy profiles in eV for the four pathways proposed in (c) with active compositions. (e) The charge difference of every active species (*COO, *COOH, CO + H_2O, HCOOH, *OCO, *OCHO, *HCOOH, and *H) on the catalyst surface. The yellow part indicates the charge accumulation and the cyan part illustrates the charge depletion.

Conclusions

In summary, this work fabricates conductive Bi–HHTP *via* the solvothermal method, and its crystal structure is first unravelled *via* single-crystal X-ray diffraction. Bi–HHTP with excellent electrical conductivity (1.65 S m^{-1}) exhibits numerous defects, which is verified by EPR. Bi–HHTP displays high selectivity to formate (95%) in a flow cell with a CEE of 68.8% and a maximum TOF of 576 h^{-1}. The *in situ* Raman spectroscopy, XRD, and XPS results further confirm its robust structure. Both *in situ* ATR-FTIR and DFT calculations confirm that the key intermediate is *COOH species. DFT calculations also confirm that the unsaturated coordination Bi sites within Bi–HHTP serve as active sites, which could promote charge transfer and lower the energy barrier (0.897 eV) for producing HCOOH. Besides, the electrocatalytic activity of Bi–HHTP is boosted by replacing the OER with the MOR, illustrating that the CO_2RR//MOR system requires less overpotential (about 400 mV) than the CO_2RR//OER to achieve a current density of 10 mA cm^{-2}. This work paves a new way into constructing highly active and stable cMOFs for high-performance CO_2RR, in terms of experimental and theoretical aspects.

Data availability

All relevant data are presented in the main text and ESI.†

Author contributions

Zengqiang Gao wrote the original draft and carried out the characterization and catalysis. Man Hou, Yongxia Shi, and Li Li participated in the characterization and helped draft the manuscript. Qisheng Sun and Zhiqiang Jiang joined the discussion of the data and gave useful suggestions. Shuyuan Yang participated in the characterization. Zhicheng Zhang, Wenjuan Yang and Wenping Hu supervised and guided the project.

Conflicts of interest

There are no conflicts to declare.

Acknowledgements

This work was supported by the National Natural Science Foundation of China (No. 22071172, 52121002, 51733004, and 21866032) and the National Key R&D Program of China (No. 2018YFA0703200). Financial support was provided by the Haihe Laboratory of Sustainable Chemical Transformations. The authors thank Prof. Jun Xu (School of Pharmaceutical Science and Technology, Tianjin University) for the analysis of single-crystal X-ray >diffraction.

Notes and references

1 S. Chu, Y. Cui and N. Liu, The path towards sustainable energy, *Nat. Mater.*, 2017, **16**, 16–22.
2 H. Xu, D. Rebollar, H. He, L. Chong, Y. Liu, C. Liu, C.-J. Sun, T. Li, J. V. Muntean, R. E. Winans, D.-J. Liu and T. Xu, Highly selective electrocatalytic CO_2 reduction to ethanol by metallic clusters dynamically formed from atomically dispersed copper, *Nat. Energy*, 2020, **5**, 623–632.
3 J. Zhang, W. Cai, F. X. Hu, H. Yang and B. Liu, Recent advances in single atom catalysts for the electrochemical carbon dioxide reduction reaction, *Chem. Sci.*, 2021, **12**, 6800–6819.
4 Y. Y. Birdja, E. Pérez-Gallent, M. C. Figueiredo, A. J. Göttle, F. Calle-Vallejo and M. T. M. Koper, Advances and challenges in understanding the electrocatalytic conversion of carbon dioxide to fuels, *Nat. Energy*, 2019, **4**, 732–745.
5 J. Li, Y. Sun and Z. Zhang, Perspective on machine learning in energy material discovery, *SmartMat*, 2023, DOI: **10.1002/smm2.1171**.
6 B. Wang, S. Chen, Z. Zhang and D. Wang, Low-dimensional material supported single-atom catalysts for electrochemical CO_2 reduction, *SmartMat*, 2022, **3**, 84–110.
7 Y. Wang, P. Han, X. Lv, L. Zhang and G. Zheng, Defect and Interface Engineering for Aqueous Electrocatalytic CO_2 Reduction, *Joule*, 2018, **2**, 2551–2582.
8 Y. Yang, M. Z. Ertem and L. Duan, An amide-based second coordination sphere promotes the dimer pathway of Mn-catalyzed CO_2-to-CO reduction at low overpotential, *Chem. Sci.*, 2021, **12**, 4779–4788.
9 S. Chu, C. Kang, W. Park, Y. Han, S. Hong, L. Hao, H. Zhang, T. W. B. Lo, A. W. Robertson, Y. Jung, B. Han and Z. Sun, Single atom and defect engineering of CuO for efficient electrochemical reduction of CO_2 to C_2H_4, *SmartMat*, 2022, **3**, 194–205.
10 J. Li, C. Wang, D. Wang, C. Yang, X. Cui, X. J. Gao and Z. Zhang, A hexacoordinated Bi^{3+}-based ellagate MOF with acid/base resistance boosting carbon dioxide electroreduction to formate, *J. Mater. Chem. A*, 2022, **10**, 20018–20023.
11 Y. Wang, L. You and K. Zhou, Origin of the N-coordinated single-atom Ni sites in heterogeneous electrocatalysts for CO_2 reduction reaction, *Chem. Sci.*, 2021, **12**, 14065–14073.
12 W. Zhang, M. Jiang, S. Yang, Y. Hu, B. Mu, Z. Tie and Z. Jin, *In situ* grown CuO_x nanowire forest on copper foam: a 3D hierarchical and freestanding electrocatalyst with enhanced carbonaceous product selectivity in CO_2 reduction, *Nano Res. Energy*, 2022, **1**, e9120033.
13 W. Yang, Y. Zhu, J. Li, Z. Chen, F. Nosheen, Q. Zhang and Z. Zhang, Understanding the dehydrogenation mechanism over iron nanoparticles catalysts based on density functional theory, *Chin. Chem. Lett.*, 2021, **32**, 286–290.
14 Y.-S. Wei, M. Zhang, R. Zou and Q. Xu, Metal-Organic Framework-Based Catalysts with Single Metal Sites, *Chem. Rev.*, 2020, **120**, 12089–12174.
15 B. An, Z. Li, Y. Song, J. Zhang, L. Zeng, C. Wang and W. Lin, Cooperative copper centres in a metal–organic framework for selective conversion of CO_2 to ethanol, *Nat. Catal.*, 2019, **2**, 709–717.
16 M. Hmadeh, Z. Lu, Z. Liu, F. Gándara, H. Furukawa, S. Wan, V. Augustyn, R. Chang, L. Liao, F. Zhou, E. Perre, V. Ozolins, K. Suenaga, X. Duan, B. Dunn, Y. Yamamto, O. Terasaki and O. M. Yaghi, New Porous Crystals of Extended Metal-Catecholates, *Chem. Mater.*, 2012, **24**, 3511–3513.
17 L. S. Xie, G. Skorupskii and M. Dincă, Electrically Conductive Metal-Organic Frameworks, *Chem. Rev.*, 2020, **120**, 8536–8580.
18 W. Yang, J. Li, X. Cui, C. Yang, Y. Liu, X. Zeng, Z. Zhang and Q. Zhang, Fine-tuning inverse metal-support interaction boosts electrochemical transformation of methanol into

formaldehyde based on density functional theory, *Chin. Chem. Lett.*, 2021, **32**, 2489–2494.

19 Z. Zhao, J. Zhang, M. Lei and Y. Lum, Reviewing the impact of halides on electrochemical CO_2 reduction, *Nano Research Energy*, 2023, **2**, e9120044.

20 Y. Zhu, Z. Gao, Z. Zhang, T. Lin, Q. Zhang, H. Liu, L. Gu and W. Hu, Selectivity regulation of CO_2 electroreduction on asymmetric AuAgCu tandem heterostructures, *Nano Res.*, 2022, **15**, 7861–7867.

21 D. Du, Q. Geng, L. Ma, S. Ren, J.-X. Li, W. Dong, Q. Hua, L. Fan, R. Shao, X. Wang, C. Li and Y. Yamauchi, Mesoporous PdBi nanocages for enhanced electrocatalytic performances by all-direction accessibility and steric site activation, *Chem. Sci.*, 2022, **13**, 3819–3825.

22 Z. Gao, C. Wang, J. Li, Y. Zhu, Z. Zhang and W. Hu, Conductive metal-organic frameworks for electrocatalysis: achievements, challenges, and opportunities, *Acta Phys.-Chim. Sin.*, 2021, **37**, 2010025.

23 Z. Meng, J. Luo, W. Li and K. A. Mirica, Hierarchical Tuning of the Performance of Electrochemical Carbon Dioxide Reduction Using Conductive Two-Dimensional Metallophthalocyanine Based Metal-Organic Frameworks, *J. Am. Chem. Soc.*, 2020, **142**, 21656–21669.

24 X.-F. Qiu, H.-L. Zhu, J.-R. Huang, P.-Q. Liao and X.-M. Chen, Highly Selective CO_2 Electroreduction to C_2H_4 Using a Metal–Organic Framework with Dual Active Sites, *J. Am. Chem. Soc.*, 2021, **143**, 7242–7246.

25 R. M. Stolz, A. Mahdavi-Shakib, B. G. Frederick and K. A. Mirica, Host–Guest Interactions and Redox Activity in Layered Conductive Metal–Organic Frameworks, *Chem. Mater.*, 2020, **32**, 7639–7652.

26 V. Rubio-Giménez, M. Galbiati, J. Castells-Gil, N. Almora-Barrios, J. Navarro-Sánchez, G. Escorcia-Ariza, M. Mattera, T. Arnold, J. Rawle, S. Tatay, E. Coronado and C. Martí-Gastaldo, Bottom-Up Fabrication of Semiconductive Metal–Organic Framework Ultrathin Films, *Adv. Mater.*, 2018, **30**, 1704291.

27 N. Wang, R. K. Miao, G. Lee, A. Vomiero, D. Sinton, A. H. Ip, H. Liang and E. H. Sargent, Suppressing the liquid product crossover in electrochemical CO_2 reduction, *SmartMat*, 2021, **2**, 12–16.

28 H. Wu, W. Zhang, S. Kandambeth, O. Shekhah, M. Eddaoudi and H. N. Alshareef, Conductive Metal-Organic Frameworks Selectively Grown on Laser-Scribed Graphene for Electrochemical Microsupercapacitors, *Adv. Energy Mater.*, 2019, **9**, 1900482.

29 C. Chen, X. Yan, R. Wu, Y. Wu, Q. Zhu, M. Hou, Z. Zhang, H. Fan, J. Ma, Y. Huang, J. Ma, X. Sun, L. Lin, S. Liu and B. Han, Quasi-square-shaped cadmium hydroxide nanocatalysts for electrochemical CO_2 reduction with high efficiency, *Chem. Sci.*, 2021, **12**, 11914–11920.

30 A. Dutta, I. Zelocualtecatl Montiel, K. Kiran, A. Rieder, V. Grozovski, L. Gut and P. Broekmann, A Tandem (Bi_2O_3 → Bimet) Catalyst for Highly Efficient ec-CO_2 Conversion into Formate: Operando Raman Spectroscopic Evidence for a Reaction Pathway Change, *ACS Catal.*, 2021, **11**, 4988–5003.

31 T. Chen, J.-H. Dou, L. Yang, C. Sun, N. J. Libretto, G. Skorupskii, J. T. Miller and M. Dincă, Continuous Electrical Conductivity Variation in M_3(Hexaiminotriphenylene)$_2$ (M = Co, Ni, Cu) MOF Alloys, *J. Am. Chem. Soc.*, 2020, **142**, 12367–12373.

32 F. P. García de Arquer, C.-T. Dinh, A. Ozden, J. Wicks, C. McCallum, A. R. Kirmani, D.-H. Nam, C. Gabardo, A. Seifitokaldani, X. Wang, Y. C. Li, F. Li, J. Edwards, L. J. Richter, S. J. Thorpe, D. Sinton and E. H. Sargent, CO_2 electrolysis to multicarbon products at activities greater than 1 A cm^{-2}, *Science*, 2020, **367**, 661–666.

33 W. Deng, L. Zhang, L. Li, S. Chen, C. Hu, Z.-J. Zhao, T. Wang and J. Gong, Crucial Role of Surface Hydroxyls on the Activity and Stability in Electrochemical CO_2 Reduction, *J. Am. Chem. Soc.*, 2019, **141**, 2911–2915.

34 Y. Shi, M. Hou, J. Li, L. Li and Z. Zhang, Cu-Based Tandem Catalysts for Electrochemical CO_2 Reduction, *Acta Phys.-Chim. Sin.*, 2022, **38**, 2206020.

35 X. Zhao, M. Huang, B. Deng, K. Li, F. Li and F. Dong, Interfacial engineering of In_2O_3/InN heterostructure with promoted charge transfer for highly efficient CO_2 reduction to formate, *Chem. Eng. J.*, 2022, **437**, 135114.

36 J. Wu, X. Li, W. Shi, P. Ling, Y. Sun, X. Jiao, S. Gao, L. Liang, J. Xu, W. Yan, C. Wang and Y. Xie, Efficient Visible-Light-Driven CO_2 Reduction Mediated by Defect-Engineered BiOBr Atomic Layers, *Angew. Chem., Int. Ed.*, 2018, **57**, 8719–8723.

37 N. Qiu, J. Li, H. Wang and Z. Zhang, Emerging dual-atomic-site catalysts for electrocatalytic CO_2 reduction, *Sci. China Mater.*, 2022, **65**, 3302–3323.